Highly flexible superconducting films with metal-decorated composite 2D materials

Pauline Ronseaux, Riadh Othmen, Dipankar Kalita, Zheng Han, Läetitia Marty, Nedjma Bendiab, Julien Renard, Vincent Bouchiat

Journal of Applied Physics ARTICLE scitation.org/journal/jap

Highly flexible superconducting films with metal-decorated composite 2D materials

Cite as: J. Appl. Phys. **126**, 165301 (2019); doi: 10.1063/1.5121615
Submitted: 29 July 2019 · Accepted: 5 October 2019 ·
Published Online: 22 October 2019

Pauline Ronseaux, Riadh Othmen, Dipankar Kalita, Zheng Han, Laëtitia Marty, Nedjma Bendiab, Julien Renard, and Vincent Bouchiat[a)]

AFFILIATIONS

Univ. Grenoble Alpes, CNRS, Grenoble INP, Institut Néel, 38000 Grenoble, France

[a)]vincent.bouchiat@neel.cnrs.fr

ABSTRACT

Graphene forms an ideal platform to realize macroscopic hybrid materials by direct physisorption of electronically-active adsorbates on top of the high-mobility bidimensional (2D) gas of charge carriers. Here, we demonstrate a novel composite multilayer based on a thin polymer film covered with a monolayer of CVD graphene on top of which a thin layer of tin is evaporated. The metal film shows dewetting and forms a self-organized network of metal nanodots electronically coupled to the graphene. The resulting macroscopic multilayered structure is a highly flexible, stable, and processable composite 2D material that exhibits tunable superconductivity at low temperature. The superconducting properties of the macroscopic composite extend over the full sample size (several square centimeters) and are comparable to the ones of a mesoscopic array of Josephson junctions prepared with similar materials. It provides an upscaling of the concept that is useful for flexible electronics.

I. INTRODUCTION

In bulk materials, combining organic and inorganic compounds has appeared as a productive method to obtain hybrid composites. The rationale behind such combination is that organic and inorganic materials usually have complementary properties that could together lead to multifunctional materials with novel features. The resulting properties go well beyond a simple combination of the individual properties of the original phases as a mutual synergy can occur and can produce new features that are lacking in the parent-constituent materials. Indeed, they depend on the size and morphology of the phases and the nature of their interaction.[1]

Many mechanical deformations, such as crumpling or twisting, are usually considered as threats to mechanical integrity of traditional materials and structures. Three dimensional (3D) composites have thus been developed and have become indispensable in engineering, where they offer the advantage of low weight but high strength and durability.[2] Examples of such realizations are numerous. For instance, the polymer industry allowed one to obtain stable and robust composite materials by incorporating inorganic building blocks into a polymer matrix.[3] Extending this idea of combining different types of materials with sometimes antagonist properties (inorganic/organic, soft/hard, conducting/insulating) down to two-dimensional (2D) materials is interesting as the low dimensionality reinforces the resilience to mechanical deformations and brings novel features that are usually absent in three dimensional composites, such as electronic quantum confinement. In that respect, graphene is ideal to form thin composite films since its absence of bulk allows maximal interaction with the other constituents and a direct virtually barrier-free electrical contact. Graphene-based composites are particularly interesting since they offer a new way to further exploit graphene exceptional properties, such as mechanical resilience, surface conductivity, and electric field effect. Theoretical works predicted the emergence of superconducting correlations in graphene decorated with arrays of superconducting islands.[4] The resulting superconducting proximity effect and its gate tunability have been demonstrated experimentally and have shown to be a source of gate tunable 2D superconductivity[5] and a model system to study the superconducting-to-insulator transition.[6] In these previous works, samples of limited area were studied. We propose here to extend this concept of tunable superconductivity up to the scale of a macroscopic material by exploring how flexible graphene-based composite films can be produced.

We propose a macroscopic flexible thin composite film formed from 3 original compounds stacked together: organic

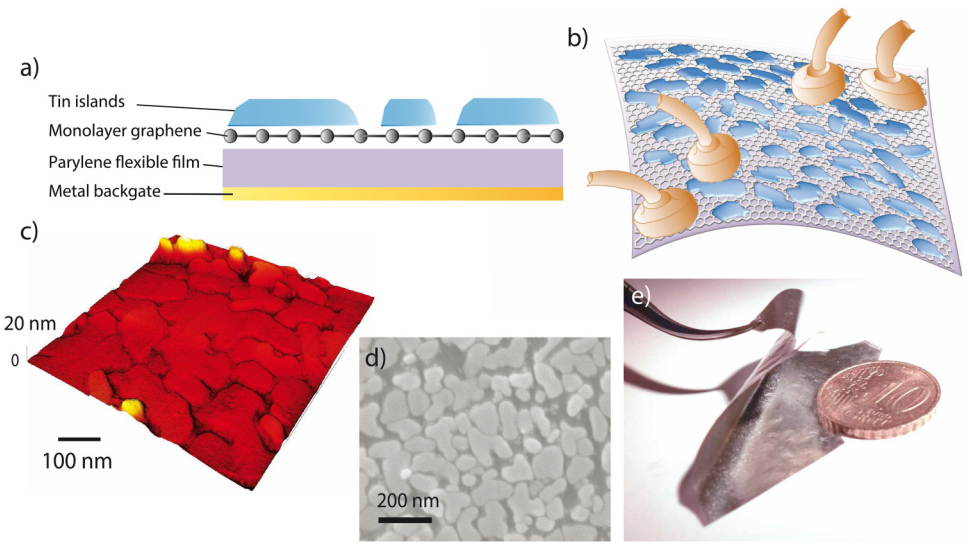

FIG. 1. Schematics of the composite film. (a) and (b) Schematics of the device showing the parylene-supported graphene decorated with the metallic tin dots. Optional back-metallization of the parylene film enables the implementation of an electrostatic gate to study the field effect of the transport properties. The contacts sketched in (b) are made using silver paint in the experiment. Their diameter is of the order of 1 mm. (c) Atomic force and (d) scanning electron micrographs of a typical sample. (e) Macrophotography of a several square centimeter superconducting flexible composite film.

(polymer plastic film) and inorganic (metal) materials are linked together through a CVD-made monolayer (ML) graphene (semimetal) sandwiched in between them. The organic polymer is composed of a few micrometer thick parylene layer, also named poly-*para*-xylylene. This chlorinated-type C parylene is a soft, stress-resilient material with bending rigidity[7] much lower than commonly used substrates such as silicon.[8] Furthermore, it can provide a mechanically stable substrate with typical thicknesses as thin as a few micrometers. The inorganic compound is based on an array of nonpercolating adsorbates made of type-I superconducting, a few nanometers thick, nanoparticles of tin (Sn). The graphene monolayer supported by the organic parylene substrate provides a two-dimensional gas of charge carriers to connect together the tin nanoparticles. The flexibility of thin parylene C substrate, reinforced by the very high mechanical strength of the graphene interface[9] and preserved by the discontinuity of the layer of tin, ensures the mechanical cohesion of the composite film. Thus, it is possible to repeatedly deform the composite film without fracturing unlike rigid materials (see Fig. 1).

In the low temperature regime, the composite film exhibits long range superconducting correlations over the whole macroscopic interface of the tin-decorated graphene. The hybrid mix between the superconducting properties of the tin-decorated graphene and the properties of the parylene substrate, including high-flexibility and thermal insulation, is typical of the plasticlike superconductors class.[2,10,11] We will show here that this new hybrid material brings an additional key characteristic: the possibility of a control with an electric field. The processability of this macroscopic composite film paves the way for applications such as flexible hybrid electronics[12,13] for thermal and vibrational insulating of cryogenic wiring and propagation of (microwave) electrical signals with minimal heat load.[14] The fabrication methods and the measurement setup will be described first. Secondly, the electronic contribution of each compound will be determined using Raman spectroscopy. Thirdly, electron transport properties will be described in detail. Finally, we will discuss the peculiar properties that appear in a perpendicular magnetic field and their potential applications.

II. TECHNIQUES AND METHODS

A. Material fabrication

The process to combine the three compounds consists in growing graphene by chemical vapor deposition (CVD) on a copper substrate[15] and depositing a several micrometer thick layer of parylene on the graphene by vaporization.[16] The copper substrate is then back-etched in a following step in order to provide a stable graphene-on-parylene film. Finally, a tin film is thermally evaporated under vacuum. Spontaneous dewetting of this metallic film leads to a random array of graphene-supported tin nanoparticles with reproducible sized gaps approximately 20 nm wide. This natural phenomenon resulting from the high surface diffusion of metal on graphene leads to a hybrid system with remarkable homogeneity avoiding any use of lithography. Details of the fabrication are provided in the supplementary material. Using other deposition conditions, such as a low temperature or the use of a sticking layer could allow one to deposit a continuous film. While this goes beyond the scope of this study, we note that it could be used to realize vertical Josephson junctions in which graphene acts as a tunnel barrier, similar to the work of Lee *et al.*[17] The composite is sketched in Fig. 1. Two samples have been studied: sample 1 (15 nm Sn/ML graphene/4 μm parylene) and sample 2 (20 nm Sn/ML graphene/10 μm parylene). Most of the results presented in the main text were obtained on sample 1. The initial samples size was tens of square centimeter. They were cut into pieces of about 1 cm^2 to fit the size of the sample holders.

B. Measurement setup

In this work, we probed the electronic properties of the samples by varying different external parameters. The cryogenic

environment was provided by a dilution refrigerator, which allowed one to vary the temperature from 100 mK up to 300 K. The direct bias current (DC) was supplied by a programable DC source (Yokogawa 7651). A superconducting coil was used to create a transverse magnetic field. The electric field, source of charge carrier modulation, was applied with a back gate on the back-metallized parylene substrate. The electrical contacts on the devices were done with silver paste. Four probes measurements of the differential resistance have been performed using standard low frequency lock-in techniques, probing area of a fraction of square centimeters.

III. RESULTS

A. Raman analysis

In order to assess the properties (doping and strain, in particular) of the graphene, both before and after tin deposition, Raman spectroscopy was performed at 532 nm on sample 1 before and after tin evaporation on top of graphene. The spectra are shown in Fig. 2(a). Before tin deposition, the Raman spectrum [red line in Figs. 2(a), 2(c), and 2(d)] exhibits several peaks corresponding to Raman modes of both graphene and parylene. The peaks at $691.6 \pm 1\,\mathrm{cm}^{-1}$, $876.1 \pm 1.7\,\mathrm{cm}^{-1}$, $913.3 \pm 1\,\mathrm{cm}^{-1}$, $1005.5 \pm 1\,\mathrm{cm}^{-1}$, $1208.9 \pm 1\,\mathrm{cm}^{-1}$, $1336.8 \pm 1\,\mathrm{cm}^{-1}$, and $1441.0 \pm 1\,\mathrm{cm}^{-1}$ are attributed to parylene C and are observed on a Parylene reference sample (see the supplementary material). The last mentioned three peaks have already been observed in previous studies reported in the literature.[19,20] The peaks at $1599.6 \pm 1\,\mathrm{cm}^{-1}$ and $2695.9 \pm 1\,\mathrm{cm}^{-1}$ correspond to the G and 2D modes of the graphene, respectively. The overlap of the G mode with a supplementary parylene C mode near $1610\,\mathrm{cm}^{-1}$ has been highlighted in the literature.[20] The G peak position has been determined by fitting the corresponding peak with a double lorentzian profile. One of the two lorentzian has been fixed at $1609.1\,\mathrm{cm}^{-1}$, which corresponds to the position of the parylene C peak extracted from a Raman spectrum measured on C parylene without graphene (see the supplementary material). Note that this procedure can induce some uncertainty on the G peak position.

After tin deposition [blue line in Figs. 2(a), 2(c), and 2(d)], the positions of the parylene C modes are essentially unaffected although their intensity is attenuated due to the screening effect induced by the metallic tin nanoparticles. The parylene C mode at $1441.0 \pm 1\,\mathrm{cm}^{-1}$ is the only one not observable after tin deposition [see Fig. 2(c)] because of its low intensity. We do not observe any signature of the graphene related D-band, which would be a signature of defect creation during tin deposition. While the presence of an emission related to parylene in this frequency range ($1350\,\mathrm{cm}^{-1}$) might mask the graphene D-band, previous studies on different substrates (for instance Si/SiO_2) have shown that deposition of tin does not create any defects in graphene.[21]

On the other hand, the G and 2D modes of graphene are shifted. Figures 2(c) and 2(d) are zoomed views of the G and 2D shifts, respectively. The wavenumbers of these two modes (ω_G; ω_{2D}) are ($1599.6 \pm 1\,\mathrm{cm}^{-1}$; $2695.9 \pm 1\,\mathrm{cm}^{-1}$) before and ($1590.3 \pm 1\,\mathrm{cm}^{-1}$; $2687.3 \pm 1\,\mathrm{cm}^{-1}$) after tin deposition. The G and 2D Raman modes (ω_G; ω_{2D}) are both sensitive to induced strain[22–25] and charge doping.[26,27] The comparison of these two modes before and after tin deposition allows us to determine to what extent each physical mechanism is responsible for their shifts.[18] The wavenumbers of the graphene Raman modes are reported in the ω_G-ω_{2D} plane featured in Fig. 2(b). The analysis presented here follows the ones

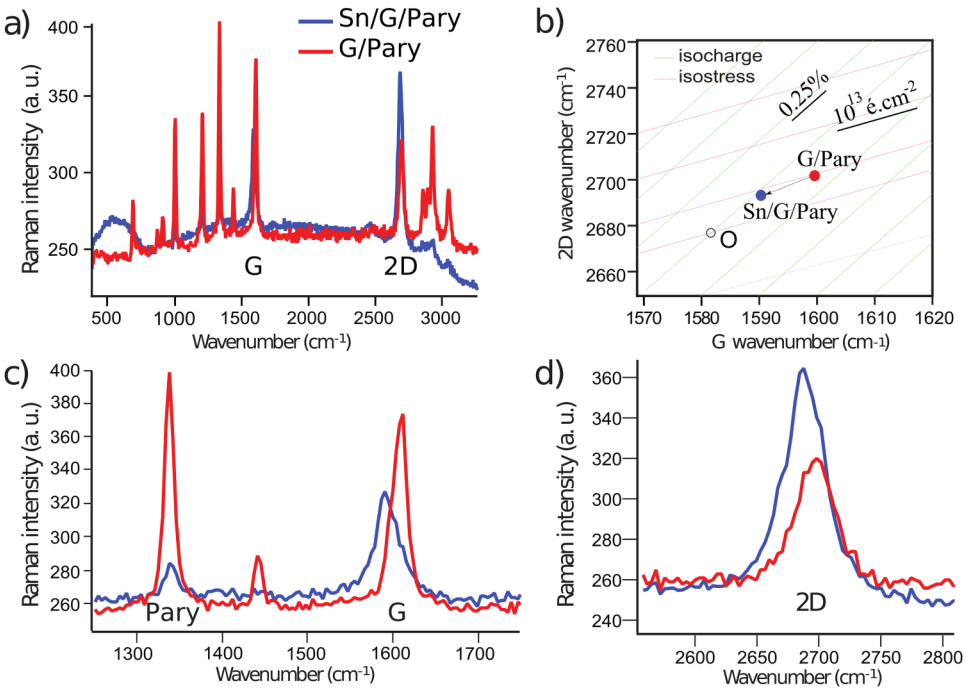

FIG. 2. Raman spectroscopy of sample 1. (a), (c) and (d) Raman spectra acquired before (red curves) and after tin deposition (blue curves) on the graphene (G)/parylene(Pary) composite film. (b) Correlation between the G and 2D Raman modes (ω_G; ω_{2D}) before (red point) and after (blue point) tin deposition. The isostress lines (magenta) with a slope of 0.7 ± 0.05 represent (ω_G; ω_{2D}) for strain-free graphene doped with varying density of holes. The isocharge lines with a slope of 2.2 ± 0.2 represent (ω_G; ω_{2D}) for graphene under variable uniaxial stress.[18] The 2D peak positions in (b) were extrapolated for an excitation at 514 nm.

developed by Lee *et al.*[18] and Das *et al.*[27] Note that the difference in laser wavelength in our study compared to Refs. 18 and 27 (532 nm vs 514 nm) was taken into account by extrapolating the 2D peak position using the reported energy dispersion for the 2D peak, i.e., 74 cm^{-1}/eV.[28]

The O point in Fig. 2(b) is the expected postition of (G;2D) peaks for a neutral stress-free graphene.[18] Starting from this origin O, strain and doping induce shifts represented by unit vectors that are nonorthogonal in the (ω_G; ω_{2D}) basis. The isostress lines (magenta) represent the effect of p-doping. The isocharge lines (green) represent a prediction of the wavenumbers (ω_G; ω_{2D}) evolution under uniaxial stress. The uniaxial strain sensitivity of the G mode is $-23.5\,cm^{-1}/\%$.[18,29] The red and blue points correspond to the experimental positions of the two modes before and after tin deposition, respectively.

From Fig. 2(b), we get an induced p-doping around $7 \cdot 10^{12}\,cm^{-2}$ and a strain of 0.35/% before tin deposition. Recent studies have reported a strong hole doping induced by parylene C.[30] The decrease of the position of the 2D mode after tin deposition is a strong indication of the increase of electron concentration in graphene[27] induced by tin, which is consistent with previous reports.[5] To precisely extract the electron concentration, we have measured the sample conductance as a function of gate voltage. The position of the neutrality peak translates into a doping of $6 \cdot 10^{12}\,cm^{-2}$. Thus, the Raman spectra after tin deposition displayed in Figs. 2(a), 2(c), and 2(d) (blue lines) ($\omega_G = 1590.3 \pm 1\,cm^{-1}$; $\omega_{2D} = 2687.3 \pm 1\,cm^{-1}$) correspond to a Fermi level above the Dirac point.

B. Temperature dependence of the conductance

Upon cooling, sample 1 exhibits a two-step transition to the superconducting state. The first resistance drop at 3.7 K in the differential resistance $\frac{dV}{dI}$ shown in Fig. 3(a) corresponds to the superconducting transition of the individual tin islands. This temperature is also the bulk critical temperature T_c of tin,[31,32] meaning that the intrinsic superconducting properties of the tin islands are almost unaffected. The composite film then reaches a resistanceless state after another wide drop at 2.4 K which corresponds to the transition of the whole tin decorated graphene sample to a superconducting state, which is driven by the superconducting proximity effect.

C. Electric field effect

The Josephson effect in graphene has been previously studied by measuring superconductor/normal/superconductor (SNS) junctions consisting of a graphene layer contacted by two superconducting electrodes.[33–35] In such systems, the superconducting proximity effect in graphene is locally generated from the contacting electrodes and gives rise to a supercurrent carried either by electrons in the conduction band or by holes in the valence band of graphene, depending on the doping. It has been shown that the proximity induced superconducting correlations can be controlled by means of a gate electrode. This gate tunable superconducting proximity effect in graphene was also demonstrated for a mesoscopic 2D network of superconducting tin clusters.[5,6] In these previous studies on graphene-based Josephson junctions arrays, the gate voltage was applied through a stiff substrate made of a silicon oxide dielectric.

As the samples of the composite film studied in this work have a surface of typically a fraction of square centimeter, $1 \cdot 10^9$ of Josephson junctions can be probed thanks to the high density of the dewetted tin islands (about 100 per micrometer square, see the supplementary material). The high breakdown voltage of the order of 1 V/nm of the parylene C,[19] its small thickness of a few micrometers, and its 20 nm gold back-metallization make it possible to apply an electric field to tune the density of the charge carriers. At low temperature, these charge carriers convey the superconducting current in graphene between the superconducting tin adsorbates.

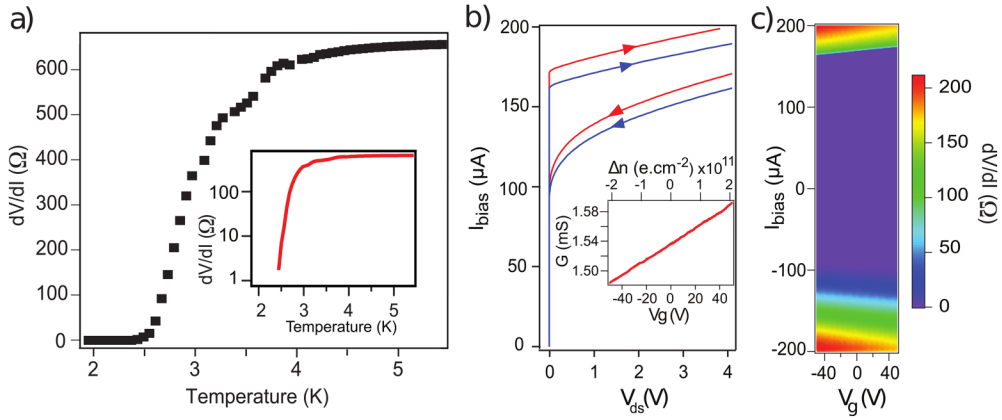

FIG. 3. Temperature and gate voltage dependence of electron transport (sample 1). (a) Temperature dependence of the differential resistance showing the gradual superconducting transition. The log scale used for the inset highlights the decrease of the differential resistance. (b) Relationship between the drain-source voltage (V_{ds}) and the bias current (I_b) at 200 mK and at two gate voltage values, $V_g = +50$ V (red curve) and $V_g = -50$ V (blue curve). The inset displays the variation of the conductance (G) with the gate voltage (V_g) at 4 K. (c) Evolution of the differential resistance with the gate voltage (V_g) and the bias current (I_b) at 200 mK.

We next focus on the field effect dependence in sample 1. We measure a variation of the conductance G by about 7% for a gate voltage (V_g) span of 100 V at 4 K, above the superconducting transition [see the inset in Fig. 3(b)]. As the parylene C substrate thickness for sample 1 is $4 \pm 0.5\,\mu$m, its estimated geometric capacitance C_s is about $6.6 \cdot 10^{-10}\,\mathrm{F\,cm^{-2}}$ (see the supplementary material). Due to residual doping, the material is n-doped in the whole gate voltage range and the neutrality point is not accessible in the inset in Fig. 3(b). The extension by proximity effect of the superconducting correlations from the vicinity of the tin islands to the whole decorated graphene interface depends on the electrostatic doping.[6] The CVD graphene charge carrier mobility of about $1600 \pm 200\,\mathrm{cm^2\,V^{-1}\,s^{-1}}$ [deduced at an electronic density of $6 \cdot 10^{12}\,\mathrm{cm^{-2}}$ from the inset in Fig. 3(b), see the supplementary material for more details] makes the graphene interface a suitable mediator to couple tin islands.

The evolution of the drain-source voltage (V_{ds}) was probed by varying the bias current (I_b) for different gate voltages (V_g) at temperature $T = 200$ mK, well below the critical temperature of tin (3.7 K)[31,32] [see Fig. 3(b)]. For a fixed gate voltage (V_g), the $I_b(V_{ds})$ curve in Fig. 3(b) features a superconducting vertical branch at zero drain-source voltage (V_{ds}). In that region, the charge carriers can flow through the whole sample without dissipation, giving rise to a supercurrent. When the bias current (I_b) is increased until the switching current (I_s), a sudden change to a resistive branch can be seen: this is the superconducting to normal state transition. This behavior is characteristic of the regime in which the energy scale for the superconducting coupling between islands that permits transport of Cooper pairs, named Josephson coupling energy E_J, is much larger than the energy scale that tends to localize charge carriers, the charging energy E_C.[36] In the superconducting state, the switching current I_s is electrically tunable as illustrated in Figs. 3(b) and 3(c). It is modulated by 100 nA/V. This modulation may be enhanced in future by reducing the thickness of the parylene substrate.

D. Hysteretic behavior

Figure 3(b) highlights the hysteretic behavior of the superconducting transition. When the bias current (I_b) is decreased from the normal resistive state to reach the superconducting state, the return to zero for the drain-source voltage (V_{ds}) only occurs at a retrapping current (I_r), which is significantly smaller than the switching current (I_s). Like the switching, the retrapping appears as a discontinuity of the $I_b(V_{ds})$ curve in Fig. 3(b). In other words, once the decorated graphene has switched to the resistive branch, it does not recover the superconducting state until the bias current is decreased to a significantly smaller retrapping current (I_r). For instance, at a gate voltage $V_g = +50$ V [red curve in Fig. 3(b)], the switching current I_s is $172\,\mu$A, whereas the retrapping current I_r is $95\,\mu$A. Hence, the curve in Fig. 3(b) is hysteretic.

The Joule power dissipation may largely contribute to that hysteretic phenomenon, as already suggested by previous studies of the self-heating of various types of superconducting weak links.[37,38] Experimental works have demonstrated that the hysteresis in a SNS junction results from the increase of the normal-metal electron temperature (T_e) once the junction switches to the resistive state by measuring an electron temperature up to more than ten times the thermal bath temperature.[39] Hysteresis is increased when the switching current (I_s) is large. As the composite film is made of an array of graphene-based junctions and exhibits a large switching current (I_s), Joule dissipation inside graphene could be one of the mechanisms responsible for the observed hysteresis. Indeed, the Joule power $Rn \cdot I_s^2$, where $R_n \approx 650\,\Omega$ and $I_s \approx 170\,\mu$A are, respectively, the normal state resistance and the switching current at 4 K and zero gate voltage, is estimated of the order of $20\,\mu$W. This value is around $2 \cdot 10^5$ times more than the one estimated by Courtois *et al.*[39] In addition, the low thermal conductivity of the parylene C substrate ($0.084\,\mathrm{W\,m^{-1}\,K^{-1}}$ at 25 °C)[40] does not allow an efficient evacuation of the resulted heat and maintains the hysteretic phenomena. The hysteresis proves that the composite film has an ultralow thermal conductivity. It may be an advantage in a cryogenic context.

E. Magnetic field dependence

Sample 1 thickness allows a high sensitivity to a magnetic field perpendicular to its plane and makes thus possible to magnetically tune the superconducting transition. As one can see in Fig. 4(c), when no bias current is applied ($I_b = 0$ nA), the magnetic field for which the SNS junction array undergoes a transition between its superconducting state and its normal state is about 100 mT. This value is the critical magnetic field H_c for sample 1. Whenever the perpendicular magnetic field is above (H_c), the SNS junctions array differential resistance ($\frac{dV}{dI}$) never falls to zero for any bias current value. The evolution of the differential resistance ($\frac{dV}{dI}$) with the bias current (I_b) for a perpendicular magnetic field just above H_c is represented by the black line in Fig. 4(b). While the critical temperature of tin islands in our device is unchanged compared to the bulk value as discussed in Sec. III B, the critical magnetic field H_c is much larger than the bulk critical magnetic field of Sn, which has been measured to be of the order of 30 mT.[41] Previous studies of tin superconductivity at the nanoscale were carried out on Sn nanostructures. These studies found no departure from the bulk critical temperature $T_c = 3.7$ K in nanostructures but in all cases found an overall increase of the critical field (H_c) with the decrease of the particle size.[42]

When no perpendicular magnetic field is applied, the density of supercurrent (J_s) can be estimated by normalizing the switching current (I_s) with the diameter of our probes of 1 mm. Since, when there is no applied perpendicular magnetic field, the switching current (I_s) is $147\,\mu$A, the density of supercurrent $J_s = 1.47 \cdot 10^2\,\mathrm{nA\,\mu m^{-1}}$. This value corresponds to the density of supercurrent measured for single Josephson junctions[43] and shows that the critical behavior of the macroscopic composite film corresponds to the one of a single Josephson junction (see the supplementary material).

IV. DISCUSSION

A. Sensitivity to magnetic field: effect of vortices motion

As shown in Fig. 4(b), for nonzero magnetic field below the critical field H_c, the composite film presents a broad transition as a

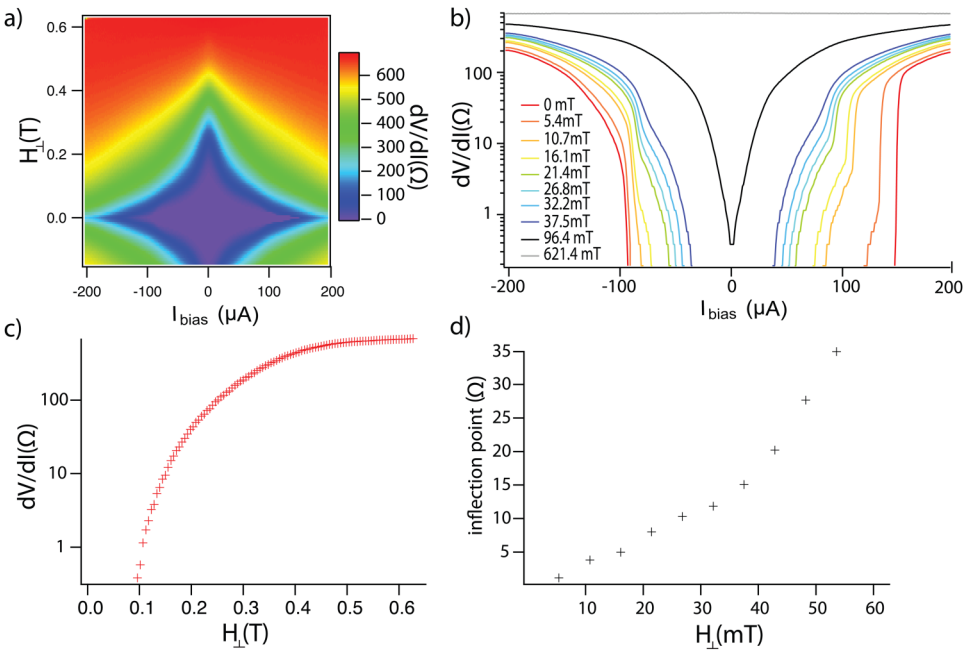

FIG. 4. Perpendicular magnetic field dependence for sample 1. (a) and (b) SNS junctions array differential resistance $\frac{dV}{dI}(I_b)$ as a function of transverse magnetic field ($H_\perp$) and bias current (I_b). (c) SNS junctions array differential resistance $\frac{dV}{dI}(I_b)$ as a function of the transverse magnetic field ($H_\perp$) in the absence of bias current ($I_b = 0$ nA). (d) SNS junctions array differential resistance $\frac{dV}{dI}(I_b)$ at the switching current I_s, i.e., at the onset of a sharp transition toward the normal state.

function of the bias current. The broadening of this transition has been attributed in previous studies to the dynamics of the vortices inducing a progressive dissipation until reaching the normal state.[44,45] Focusing on the transition from the superconducting to the normal state in the presence of magnetic field in the positive bias current quadrant, we can notice four regions, as delimited in Fig. 5(a). In the low bias current regime, i.e., region 1 in Fig. 5(a), the vortices are pinned and the composite film has zero differential resistance. Numerical simulations have studied the impact of defects in this context.[46,47] The enhancement of the superconducting current near the tip of the defects gives rise to the formation of vortices that remain pinned to each end of the defects. In our case, the defects could be regions with weaker superconducting state. When the bias current (I_b) reaches the depinning current (I_d), the Lorentz force perpendicular to the bias current (I_b) is high enough to unpin and thus governs the vortices motion.[47] Their creeping produces a voltage across the sample, which begins to present a nonzero differential resitance that increases with the bias current (I_b). We attribute the hill-shaped beginning of the transition in region 2 to this creeping regime. The macroscopic switching current (I_s) is identified as the inflection point ending regions 2, i.e., when a sharp transition toward the normal state begins. In region 2, the hill-shaped curve does not end with a plateau as it has been observed experimentally in other types of Josephson junctions arrays.[44] It means that the motion of the vortices does not reach a constant speed before entering region 3. In region 4, the curve converges progressively toward the normal state differential resistance value. There is no peak in the resistance close to the switching current (I_s) as often observed in Josephson junctions. This is likely caused by the importance of thermal effects, and such behavior has already been observed in tin-decorated graphene hybrids.[5]

When the applied magnetic field is increased, the differential resistance ($\frac{dV}{dI}$) at the macroscopic switching current (I_s) featured in Fig. 4(d) is larger and the transition displayed in Fig. 4(b) broadens. As each vortex carries a quantum of flux,[47] the increase of the applied magnetic field induces the proliferation of the number of vortices. Therefore, the magnetic field dependency of the superconducting transition as seen in Fig. 5(a) provides strong evidence for vortex-dominated electrical properties of the tin-decorated graphene.

B. Comparison of samples

Figure 5(d) shows the response to a perpendicular magnetic field for two samples, sample 1 and sample 2. For weak magnetic fields, the normalized depinning current (I_d) of sample 2 decreases more abruptly when the absolute value of the perpendicular magnetic field is increased. This enhanced sensitivity can be attributed to the arrangement of the tin islands. Indeed, the larger the pancakelike tin islands are, the closer they are. The magnetic field expelled by the Meissner effect in the tin islands is more confined in the interstitial area in graphene at the core of each Josephson junction. Since more tin was deposited on sample 2, the interstitial areas are narrower than for sample 1. It results in a strong magnetic field focusing effect in the weak link regions. This strong sensitivity of the depinning current (I_d) to small magnetic fields applied perpendicular to the film is typical for weak links.[48] Nevertheless, out of the weak magnetic field regime, the normalized depinning current (I_d) for sample 2 is higher than for sample 1. Thus, for higher values of the magnetic field, the greater surface covering of graphene by the tin islands for sample 2 compensates the effect of magnetic field confinement. The critical magnetic field (H_c) is

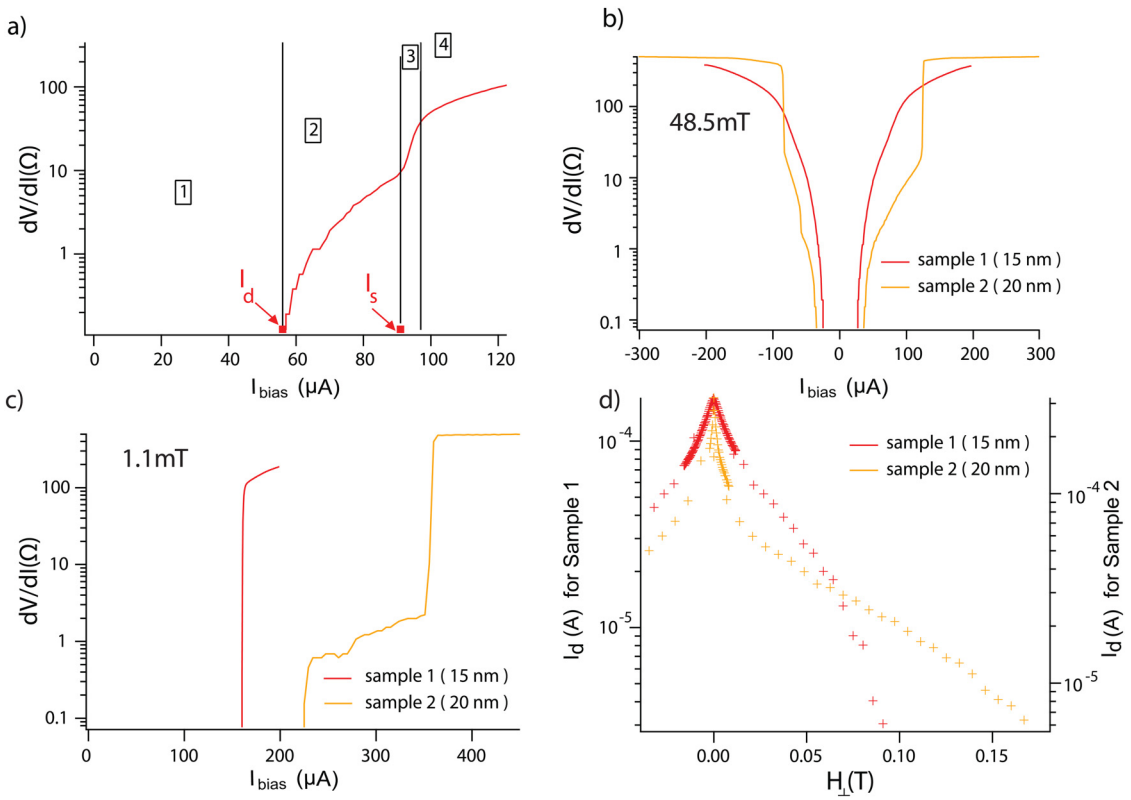

FIG. 5. Vortices motion effect and dependence with metal thickness. (a) Vortices motion dependent superconducting transition in sample 1. (b) Hysteretic behavior of the superconducting transition for sample 1 (red curve) and sample 2 (orange curve) ($H_\perp = 48.5$ mT). (c) Superconducting transition for sample 1 (red curve) and sample 2 (orange curve) at weak magnetic field ($H_\perp = 1.1$ mT). (d) Evolution of depinning current (I_d) with the perpendicular magnetic field.

more than twice higher for sample 2 compared to sample 1. Although the surfaces and aspect ratios of the two samples are of the same order, the switching current (I_s) measured at weak perpendicular magnetic field ($H_\perp = 1.1$ mT) for sample 2 was also about more than twice larger than the one of sample 1 as can be seen in Fig. 5(c). These observations are consistent with the fact that the Josephson junctions are shorter in sample 2 for which more tin has been evaporated than in sample 1.

The emergence of a large plateau in the superconducting transition of the sample 2 shown in Fig. 5(c) corresponds to a regime where the vortices reach a constant speed of motion giving rise to a constant value for the probed differential resistance. This plateau is absent for the same value of perpendicular magnetic field for the superconducting transition of the sample 1 in Fig. 5(c) because the smaller value of the switching current I_s induces a sharp transition toward the resistive normal state before the vortices reach their constant motion speed regime.

The transition from the resistive normal state to the superconducting state has not exactly the same shape as the transition from the superconducting state to the resistive normal state as one can see in Fig. 5(b). This hysteretic behavior is stronger for sample 2 because of the larger thickness of both the superconducting tin islands and the parylene substrate that prevent the heat from being efficiently evacuated.

V. CONCLUSIONS

In conclusion, we built a mechanically-flexible graphene-based metal coated thin film exhibiting tunable superconducting properties at low temperature. The noncovalent coupling of the graphene two interfaces with the top and bottom components allows the graphene to keep its exceptional electronic properties, while gaining other properties like superconductivity. This original architecture provides complementary properties such as high electrical conductivity combined with low thermal conductivity. The sensitivity to the external environment is enhanced thanks to the hybrid 2D behavior of the film. In particular, the superconducting correlations in the graphene interface are highly sensitive to a perpendicular magnetic field and electrically tunable thanks to the preserved semimetallic properties and the 2D character of the graphene. This work highlights the potential of graphene as a versatile building-block for the realization of macroscopic plasticlike superconductors with high supercurrent density comparable to single Josephson junctions. The very low volumic mass of parylene C (1.289 g cm^{-3})

allows us to get superconducting films with very low area density (about 5 g m^{-2}) compared to a pure tin thin film of the same thickness whose weight would be six times higher. Flexible superconducting thin composite films could provide a physically-compact flexible flat cable, easily processable by plasma etching into multiwires. Flexibility and superconductivity, respectively, provide vibrational and thermal insulation useful for a multistage cryostat.[14] Nevertheless, at this point, the relatively low superconducting critical temperature obtained using tin (around 2.4 K) is relatively limited compared to standard materials used in superconducting wires (18 K for Nb_3Sn) and should motivate the exploration of other materials.

On a more fundamental side, this material offers a novel playground to study the collective proximity effect at the macroscopic scale. In future, to unveil the full potential of this hybrid material as a flexible superconductor,[49] one should explore the possibility of maintaining the superconducting character when applying mechanical stress to the film. Parylene might not be the ideal candidate to handle a large stretch, compared to, for instance, polydimethylsiloxane, but for limited strains it has recently been shown that graphene/parylene C composites present very resilient electrical properties.[16]

SUPPLEMENTARY MATERIAL

See the supplementary material for details about fabrication methods and additional data on sample 1 and sample 2.

ACKNOWLEDGMENTS

J.R. acknowledges support from Grenoble Alpes University community (AGIR-2016-SUGRAF). The authors are grateful for the help from NanoFab team of Institut Néel. This work is partially supported by the French ANR Contracts GRAPHMET, CLEANGRAPH, and DIRACFORMAG and the EU GRAPHENE Flagship.

REFERENCES

[1]P. Judeinstein and C. Sanchez, "Hybrid organic–inorganic materials: A land of multidisciplinarity," J. Mater. Chem. **6**, 511–525 (1996).
[2]C. O. Oriakhi, "Polymer nanocomposition approach to advanced materials," J. Chem. Educ. **77**, 1138 (2000).
[3]M. Carraro and S. Gross, "Hybrid materials based on the embedding of organically modified transition metal oxoclusters or polyoxometalates into polymers for functional applications: A review," Materials **7**, 3956–3989 (2014).
[4]M. V. Feigel'man, M. A. Skvortsov, and K. S. Tikhonov, "Proximity-induced superconductivity in graphene," JETP Lett. **88**, 747–751 (2008).
[5]B. M. Kessler, Ç. Ö. Girit, A. Zettl, and V. Bouchiat, "Tunable superconducting phase transition in metal-decorated graphene sheets," Phys. Rev. Lett. **104**, 1–4 (2010).
[6]A. Allain, Z. Han, and V. Bouchiat, "Electrical control of the superconducting-to-insulating transition in graphene-metal hybrids," Nat. Mater. **11**, 1–5 (2012).
[7]R. P. Von Metzen and T. Stieglitz, "The effects of annealing on mechanical, chemical, and physical properties and structural stability of Parylene C," Biomed. Microdevices **15**, 727–735 (2013).
[8]M. A. Hopcroft, W. D. Nix, and T. W. Kenny, "What is the Young's modulus of silicon?," J. Microelctromech. Syst. **19**, 229–238 (2010).
[9]C. Lee, X. Wei, J. W. Kysar, and J. Hone, "Measurement of the elastic properties and intrinsic strength of monolayer graphene," Science **321**, 385–388 (2008).
[10]H.-l. Tsai, J. L. Schindler, C. R. Kannewurf, and M. G. Kanatzidis, "Plastic superconducting polymer-$NbSe_2$ nanocomposites," Chem. Mater. **9**, 875–878 (1997).
[11]M. Kryszewski, "Nanointercalates—Novel class of materials with promising properties," Synth. Met. **109**, 47–54 (2000).
[12]M. Caironi, T. D. Anthopoulos, Y.-Y. Noh, and J. Zaumseil, "Organic and hybrid materials for flexible electronics," Adv. Mater. **25**, 4208–4209 (2013).
[13]D. B. Mitzi, K. Chondroudis, and C. R. Kagan, "Organic–inorganic electronics," IBM J. Res. Dev. **45**, 29–45 (2001).
[14]D. B. Tuckerman, M. C. Hamilton, D. J. Reilly, R. Bai, G. A. Hernandez, J. M. Hornibrook, J. A. Sellers, and C. D. Ellis, "Flexible superconducting Nb transmission lines on thin film polyimide for quantum computing applications," Supercond. Sci. Technol. **29**, 084007 (2016).
[15]X. Li, W. Cai, J. An, S. Kim, J. Nah, D. Yang, R. Piner, a. Velamakanni, I. Jung, E. Tutuc, S. K. Banerjee, L. Colombo, and R. S. Ruoff, "Large-area synthesis of high-quality and uniform graphene films on copper foils," Science **324**, 1312–1314 (2009).
[16]M. Kim, A. Shah, C. Li, P. Mustonen, J. Susoma, F. Manoocheri, J. Riikonen, and H. Lipsanen, "Direct transfer of wafer-scale graphene films," 2D Mater. **4**, 035004 (2017).
[17]G.-H. Lee, S. Kim, S.-H. Jhi, and H.-J. Lee, "Ultimately short ballistic vertical graphene Josephson junctions," Nat. Commun. **6**, 6181 (2015).
[18]J. E. Lee, G. Ahn, J. Shim, Y. S. Lee, and S. Ryu, "Optical separation of mechanical strain from charge doping in graphene," Nat. Commun. **3**, 1024 (2012).
[19]J. Jakabovič, J. Kováč, M. Weis, D. Haško, R. Srnánek, P. Valent, and R. Resel, "Preparation and properties of thin parylene layers as the gate dielectrics for organic field effect transistors," Microelectronics J. **40**, 595–597 (2009).
[20]D.-W. Park, S. K. Brodnick, J. P. Ness, F. Atry, L. Krugner-Higby, A. Sandberg, S. Mikael, T. J. Richner, J. Novello, H. Kim, D.-H. Baek, J. Bong, S. T. Frye, S. Thongpang, K. I. Swanson, W. Lake, R. Pashaie, J. C. Williams, and Z. Ma, "Fabrication and utility of a transparent graphene neural electrode array for electrophysiology, in vivo imaging, and optogenetics," Nat. Protocols **11**, 2201–2222 (2016).
[21]A. Allain, Ph.D. thesis, Joseph Fourier University, Grenoble, 2012.
[22]M. Huang, H. Yan, C. Chen, D. Song, T. F. Heinz, and J. Hone, "Phonon softening and crystallographic orientation of strained graphene studied by Raman spectroscopy," Proc. Natl. Acad. Sci. U.S.A. **106**, 7304–7308 (2009).
[23]M. Huang, H. Yan, T. F. Heinz, and J. Hone, "Probing strain-induced electronic structure change in graphene by Raman spectroscopy," Nano Lett. **10**, 4074–4079 (2010).
[24]T. M. G. Mohiuddin, A. Lombardo, R. R. Nair, A. Bonetti, G. Savini, R. Jalil, N. Bonini, D. M. Basko, C. Galiotis, N. Marzari, K. S. Novoselov, A. K. Geim, and A. C. Ferrari, "Uniaxial strain in graphene by Raman spectroscopy: *G* peak splitting, Grüneisen parameters, and sample orientation," Phys. Rev. B **79**, 205433 (2009).
[25]N. Bendiab, J. Renard, C. Schwarz, A. Reserbat-Plantey, L. Djevahirdjian, V. Bouchiat, J. Coraux, and L. Marty, "Unravelling external perturbation effects on the optical phonon response of graphene," J. Raman Spectrosc. **49**, 130–145 (2018).
[26]J. Yan, Y. Zhang, P. Kim, and A. Pinczuk, "Electric field effect tuning of electron-phonon coupling in graphene," Phys. Rev. Lett. **98**, 166802 (2019).
[27]A. Das, S. Pisana, B. Chakraborty, S. Piscanec, S. K. Saha, U. V. Waghmare, K. S. Novoselov, H. R. Krishnamurthy, A. K. Geim, A. C. Ferrari, and A. K. Sood, "Monitoring dopants by Raman scattering in an electrochemically top-gated graphene transistor," Nat. Nanotechnol. **3**, 210–215 (2008).
[28]R. Narula and S. Reich, "Double resonant Raman spectra in graphene and graphite: A two-dimensional explanation of the Raman amplitude," Phys. Rev. B **78**, 165422 (2008).
[29]D. Yoon, Y.-W. Son, and H. Cheong, "Strain-dependent splitting of the double-resonance Raman scattering band in graphene," Phys. Rev. Lett. **106**, 155502 (2011).

[30]G. Skoblin, J. Sun, and A. Yurgens, "Encapsulation of graphene in Parylene," Appl. Phys. Lett. **110**, 3–7 (2017).
[31]B. Matthias, T. Geballe, and V. Compton, "Superconductivity," Rev. Mod. Phys. **35**, 1–22 (1963).
[32]J. Eisenstein, "Superconducting elements," Rev. Mod. Phys. **26**, 277–291 (1954).
[33]H. B. Heersche, P. Jarillo-Herrero, J. B. Oostinga, L. M. K. Vandersypen, and A. F. Morpurgo, "Bipolar supercurrent in graphene," Nature **446**, 56–59 (2007).
[34]X. Du, I. Skachko, and E. Y. Andrei, "Josephson current and multiple Andreev reflections in graphene SNS junctions," Phys. Rev. B **77**, 184507 (2008).
[35]K. Komatsu, C. Li, S. Autier-Laurent, H. Bouchiat, and S. Guéron, "Superconducting proximity effect in long superconductor/graphene/superconductor junctions: From specular Andreev reflection at zero field to the quantum Hall regime," Phys. Rev. B **86**, 115412 (2012).
[36]H. V. D. Zant, W. J. W. Elion, L. J. Geerligs, J. E. Mooij, H. S. J. van der Zant, W. J. W. Elion, L. J. Geerligs, and J. E. Mooij, "Quantum phase transitions in two dimensions: Experiments in Josephson-junction arrays," Phys. Rev. B **54**, 10081–10093 (1996).
[37]T. a. Fulton and L. N. Dunkleberger, "Origin of hysteresis in the I-V curves of point-contact junctions," J. Appl. Phys. **45**, 2283–2285 (1974).
[38]W. J. Skocpol, M. R. Beasley, and M. Tinkham, "Self heating hotspots in superconducting thin film microbridges," J. Appl. Phys. **45**, 4054–4066 (1974).
[39]H. Courtois, M. Meschke, J. T. Peltonen, and J. P. Pekola, "Origin of hysteresis in a proximity Josephson junction," Phys. Rev. Lett. **101**, 1–4 (2008).
[40]See http://www.vp-scientific.com/parylene_properties.htm for "Parylene Properties and Characteristics" (last accessed: March 30, 2018).
[41]R. W. Shaw, D. E. Mapother, and D. C. Hopkins, "Critical fields of superconducting tin, indium, and tantalum," Phys. Rev. **120**, 88–91 (1960).
[42]Y. J. Hsu, S. Y. Lu, and Y. F. Lin, "Nanostructures of Sn and their enhanced, shape-dependent superconducting properties," Small **2**, 268–273 (2006).
[43]V. E. Calado, S. Goswami, G. Nanda, M. Diez, A. R. Akhmerov, K. Watanabe, T. Taniguchi, T. M. Klapwijk, and L. M. Vandersypen, "Ballistic Josephson junctions in edge-contacted graphene," Nat. Nanotechnol. **10**, 761–764 (2015).
[44]M. Durkin, I. Mondragon-Shem, S. Eley, T. L. Hughes, and N. Mason, "History-dependent dissipative vortex dynamics in superconducting arrays," Phys. Rev. B **94**, 1–8 (2016).
[45]W. Xia and P. L. Leath, "Defects, vortices, and critical current in Josephson-junction arrays," Phys. Rev. Lett. **63**, 1428–1431 (1989).
[46]P. L. Leath and W. Xia, "Vortices and critical current in disordered arrays of Josephson junctions," Phys. Rev. B **44**, 9619–9633 (1991).
[47]L. Gor'kov and N. Kopnin, "Vortex motion and resistivity of type-ll superconductors in a magnetic field," Uspekhi Fizicheskih Nauk **116**, 413 (1975).
[48]J. Mannhart, P. Chaudhari, D. Dimos, C. C. Tsuei, and T. R. McGuire, "Critical currents in [001] grains and across their tilt boundaries in $YBa_2Cu_3O_7$ films," Phys. Rev. Lett. **61**, 2476–2479 (1988).
[49]M. R. Koblischka, X. L. Zeng, T. Karwoth, T. Hauet, and U. Hartmann, "Magnetic properties of electrospun non-woven superconducting fabrics," AIP Adv. **6**, 035115 (2016).